

Solar Wind Control of Hemispherically-Integrated Field-Aligned Currents at Earth

A. L. Fleetham¹, S. E. Milan¹, S. M. Imber¹, S. K Vines²

¹School of Physics and Astronomy, University of Leicester, UK

²Johns Hopkins University Applied Physics Laboratory, USA

Key Points:

- Solar wind-magnetosphere-ionosphere coupling
- Solar wind driving of field-aligned currents
- Cross polar cap potential/ current saturation

Corresponding author: A. L. Fleetham, Alf21@leicester.ac.uk

Abstract

Magnetic reconnection occurring between the interplanetary magnetic field and the dayside magnetopause causes a circulation of magnetic flux and plasma within the magnetosphere, known as the Dungey cycle. This circulation is transmitted to the ionosphere via field-aligned currents (FACs). The magnetic flux transport within the Dungey cycle is quantified by the cross-polar cap potential (CPCP or transpolar voltage). Previous studies have suggested that under strong driving conditions the CPCP can saturate near a value of 250 kV. In this study we investigate whether an analogous saturation occurs in the magnitudes of the FACs, using observations from the Active Magnetosphere and Planetary Electrodynamics Response Experiment (AMPERE). The solar wind speed, density and pressure, the B_z component of the interplanetary magnetic field, and combinations of these, were compared to the concurrent integrated current magnitude, across each hemisphere. We find that FAC magnitudes are controlled most strongly by solar wind speed and the orientation and strength of the interplanetary magnetic field. FAC magnitude increases monotonically with solar wind driving but there is a distinct knee in the variation around IMF $B_z = -10$ nT, above which the increase slows.

Plain Language Summary

During extreme space weather events, the threat to space-based and surface infrastructure has become of increasing concern within the past 2 decades. These space weather events are directly responsible for electrical currents flowing in the ionosphere that produce potentially dangerous magnetic field perturbations on the ground. With this motivation, we use satellite magnetometer data in order to gain greater insight into the field aligned current systems present above both poles of the Earth. With many mechanisms and processes which govern the magnitude of these currents (and associated potentials) still being widely disputed, we hope to offer verification of whether or not these currents saturate at high solar wind driving, in order to create a clearer picture of the behaviour of these systems from nominal to intense space weather conditions.

1 Introduction

Observations of the strength of ionospheric convection, parameterised by the cross polar cap potential (CPCP), are often used as a measure of the strength of solar wind-magnetosphere coupling. Under normal conditions the CPCP is found to be approximately linearly-related to the solar wind motional electric field, once corrected for interplanetary magnetic field (IMF) clock angle which modulates the reconnection geometries available at the magnetopause (Khachikjan et al., 2008). However, it is observed that under particularly strong driving conditions the CPCP saturates (Hairston et al., 2005; Shepherd, 2007; Russell et al., 2001). Several competing theories have been put forward to explain saturation, including induced magnetospheric magnetic fields opposing that of the magnetopause, limiting the global reconnection rate, and Alfvén wave impedance (mismatching) at the ionosphere (Gao et al., 2013; Siscoe et al., 2002; Kivelson & Ridley, 2008).

A significant hurdle to better understanding this phenomenon is the relative rarity of sufficiently strong solar wind driving conditions and the difficulty of accurately measuring the CPCP at such times. Measurements of the CPCP by low Earth orbit spacecraft, such as those of Defense Meteorological Satellite Program (DMSP), and by ground-based ionospheric radars, such as the Super Dual Auroral Radar Network (SuperDARN), can be unreliable during geomagnetically disturbed conditions. In this study we use observations of the field-aligned currents (FACs) measured by the Active Magnetosphere and Planetary Electrodynamics Response Experiment (AMPERE) as a diagnostic for convection strength. Initial studies, such as that undertaken by Anderson and Korth (2007), have suggested that this saturation of the current does occur. Their study employed en-

gineering magnetic field data from the Iridium Communications Network satellite constellation from 1999 to 2003 and looked at the evolution of FACs during instances of geomagnetic storms. In this study, we also use data from AMPERE, in tandem with solar wind observations from the OMNI data set, to investigate the field-aligned current systems over both hemispheres, with increasing solar wind driving. Building on this previous study, we employ AMPERE data from the seven years of 2010 to 2016. By not limiting the data analysed to just storm-time conditions, we provide a fuller picture of how the integrated current magnitude behaves in response to increasing solar wind driving from nominal to extreme conditions.

2 Data Sets

The AMPERE dataset comprises polar maps of field-aligned current density derived from magnetometer observations made onboard satellites of the Iridium telecommunications constellation (Anderson et al., 2002; Waters et al., 2020, 2001). Measured perturbations from the background magnetic field are inverted with Ampère’s law to retrieve the FAC density on a grid of 24 hours of magnetic local time and 50 1-degree magnetic latitude bins, over both northern and southern polar regions. The AMPERE-derived FAC distributions are comprised of a 10-minute interval of observations that span the polar regions. The FAC patterns can then be produced at a 2-minute cadence using a sliding 10-minute accumulation window (Anderson et al., 2002; Waters et al., 2020).

The aim of this study is to determine the relationship between AMPERE observations of FACs and upstream solar wind conditions. The solar wind parameters considered were the solar wind speed, density and pressure, and the Geocentric Solar Magnetospheric (GSM) B_y and B_z components of the IMF at the nose of the bowshock, all provided by the OMNI data set (King & Papitashvili, 2005). From these we derived the Y-component of the motional electric field of the solar wind, $E_y = -V_{sw}B_z$, a measure of the magnetic flux transported within the solar wind towards the magnetosphere which can reconnect with Earth’s dipole. This is defined such that when $E_y > 0$ reconnection is expected at low to mid-latitudes across the dayside magnetopause which opens magnetic flux and drives the Dungey cycle; when $E_y < 0$ then reconnection is expected to occur at the high latitude magnetopause, tailwards of the cusps, known as lobe reconnection (e.g. (Fuselier, 2021) and references therein). In addition to the individual solar wind parameters, the Milan et al. (2012) coupling parameter provides an estimation of the dayside reconnection rate:

$$\Phi_D = \Lambda V_x^{\frac{4}{3}} B_{YZ} \sin^{\frac{9}{2}} \frac{1}{2} \theta \quad (1)$$

Here, Λ is a constant of proportionality with the value $3.3 \times 10^5 \text{ m}^{\frac{2}{3}} \text{ s}^{\frac{2}{3}}$. V_x is the absolute magnitude of the x-component of the solar wind velocity and B_{yz} is defined as $B_{yz} = \sqrt{B_y^2 + B_z^2}$, such that $V_x B_{yz}$ gives the transport of magnetic flux per unit length, transverse to the flow direction. Finally, θ is the IMF clock angle. When combined in this way, these parameters give an approximation of the subsolar reconnection rate, which drives the Dungey cycle, and is zero for purely northwards IMF. The analysis covers the 2010 to 2016 time period (inclusive) and aims to capture all the currents associated with the electrodynamics of magnetosphere-ionosphere coupling.

3 Observations

From the AMPERE data, we determined the integrated FAC in both the northern and southern hemispheres at 2-minute cadence. AMPERE provides field-aligned current density on a 24×50 grid in both hemispheres, with positive and negative current densities representing upward and downward FACs, respectively. In this paper we present

the results from the northern hemisphere only. The analysis was performed for the southern hemisphere, also, however the results were very similar, though the FAC magnitudes were somewhat lower, as reported by Coxon et al. (2016). The FACs are expected to be in balance such that the total FAC flowing into each hemisphere should be zero, so we treated upward and downward FACs separately. The area of each grid cell was calculated, multiplied by the FAC density in that cell, and then summed over the grid to provide a measure of the total upward and total downward FAC. Any current density of less than $0.1 \mu\text{A m}^{-1}$ was not included within the analysis, as this is close to the noise floor of the AMPERE technique. We found, as expected, that the magnitudes of the integrated upward and downward FACs were equal, and henceforth just the total FAC magnitude was used (the sum of the absolute upward and downward FAC). To determine how current magnitude varied in response to different solar wind parameters, the total current was plotted against each solar wind parameter, in addition to E_y and Φ_D . Initially separated the analysis of these parameters by year and month to determine if any seasonal or solar cycle trends were present. The FAC magnitudes differed with season due to variations in solar-insolation of the polar regions and hence conductance (Coxon et al., 2016). However, all showed the same behaviour, and we have therefore combined together the data, from all years and months, to increase statistical significance.

3.1 Quadrants and Direction of Current

We next tested to see if the response of the FACs to the solar wind differed in different local time sectors. We divided the observations into four quadrants, encompassing 03 to 09 MLT (dawn), 09 to 15 MLT (noon), 15 to 21 MLT (dusk), and 21 to 03 MLT (midnight). We then found the total upward and downward FACs in each of these quadrants. From previous studies of FACs associated with different solar wind driving conditions (Milan et al., 2017; Iijima & Potemra, 1976a; Ganushkina et al., 2018), the R1 and R2 FACs are expected to be mainly contained in the dawn and dusk quadrants, that R0 FACs would be contained in the noon quadrant, and substorm currents in the midnight quadrant. Figure 1 shows typical examples of FAC distributions for northward and southward IMF, with pink lines demarcating the four quadrants. For northward IMF the currents are located at high latitudes, predominantly confined to the noon quadrant. The currents show a quadrupolar configuration of upward and downward FACs which is typical of reverse lobe convection cells driven by lobe reconnection (Zanetti et al., 1984; Milan et al., 2020; Fear, 2021). For southward IMF the FACs are seen at lower latitudes and generally have the region 1 / region 2 configuration first described by Iijima and Potemra (1976b), which is associated with standard twin-cell convection driven by subsolar reconnection. In the example shown in Figure 1 (right panel) there is little current flowing in the noon quadrant for this particular example, however R0 FACs often appear here when B_y is non-zero. A more complicated pattern is seen in the midnight quadrant, where FACs associated with the Harang discontinuity are usually seen (Erickson et al., 1991). As these typical current patterns are so different, for many aspects of the subsequent analysis, we subdivided the dataset into observations for which $B_z > 0$ and $B_z < 0$.

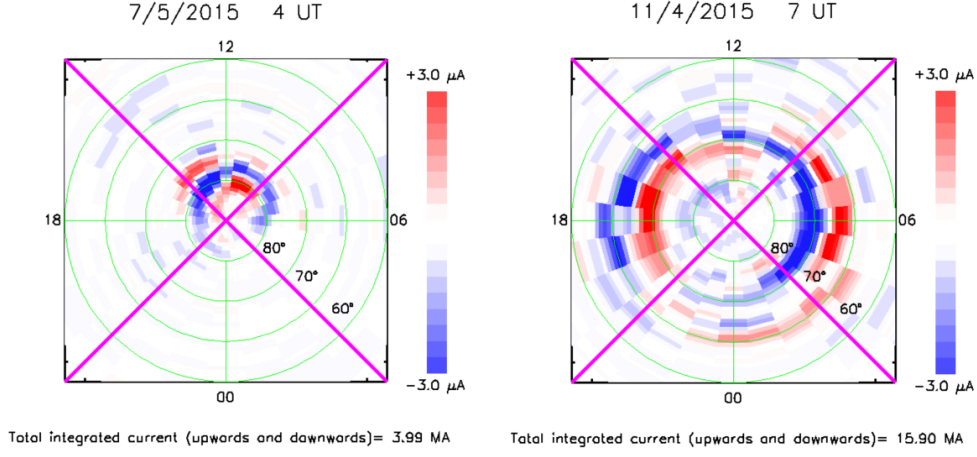


Figure 1. Current systems present above the northern hemisphere of Earth during periods of northwards (left) and southwards (right) IMF occurring on 7th May 2015 and 11th April 2015, respectively. The flow of current, towards or away from the Earth, is indicated in the blue and red shading, respectively. The pink lines indicate the division into 4 local time quadrants that was employed for the study.

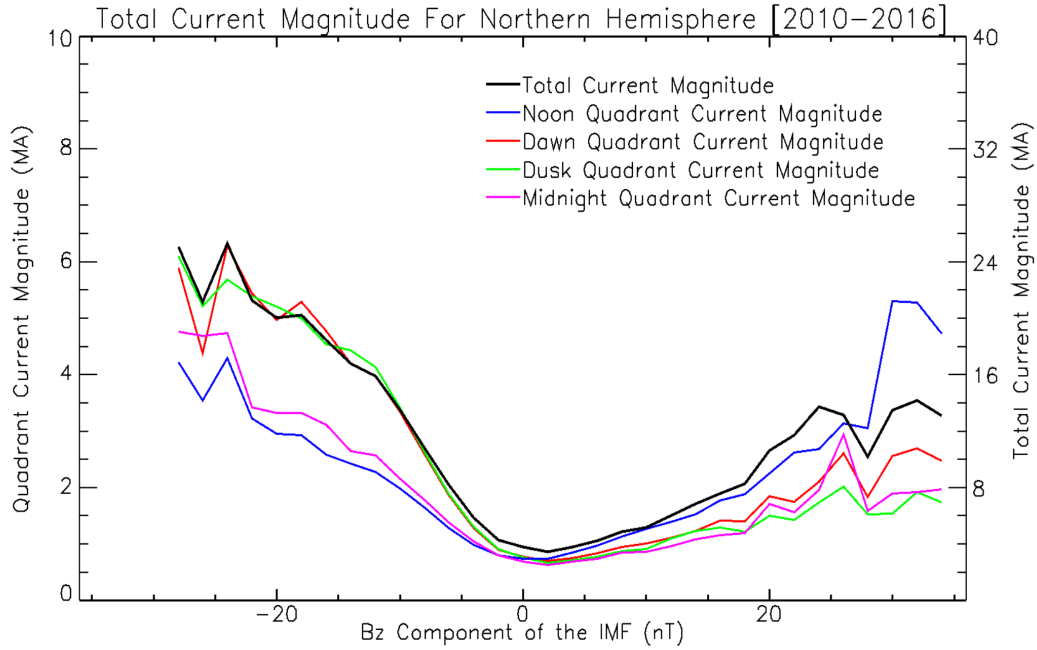


Figure 2. The total integrated current magnitudes (absolute magnitude of upwards and downwards flowing current summed) are plotted against the corresponding value of IMF B_z . The blue, pink, green and red shaded lines indicate the current magnitudes in the Noon, Midnight, Dusk and Dawn quadrants, respectively, with the left axis denoting scale. The black shaded line indicates the total current magnitude, with the right axis giving scale.

Figure 2 shows the average variation in the FAC magnitude in the northern hemisphere as a function of IMF B_z , in bins 1 nT wide, for 2010 to 2016. The FAC in each quadrant is shown by the coloured lines and the total FAC by the black line. Standard deviations of the variation are also calculated, but not shown at this stage for clarity. The FACs are a minimum for small B_z and increase as B_z becomes more negative and more positive. The increase in each quadrant is approximately linear in the range $-15 > B_z > 15$ nT. Deviations from this quasi-linearity are discussed further below. For $B_z < 0$ the FAC magnitude is smallest at noon and largest at dawn and dusk, with this trend reversed for $B_z > 0$, as expected from the representative patterns shown in Figure 1. In addition to this, the gradient is larger for $B_z < 0$, which again is to be expected. Despite the different rate of increase in the different quadrants, they all show the same quasi-linear trend, and so in the rest of the analysis we use the total FAC as the measure of current flow. During periods of northward IMF, the noon sector of each hemisphere was seen to provide the dominant contribution of current magnitude, as would be expected when considering the example shown in Figure 1 and the dynamics leading to high-latitude, dayside FACs during northward IMF. Consistency with Figure 1 is also demonstrated during periods of southward IMF. Here, the dawn and dusk quadrants were shown to provide the highest contribution to overall current magnitude for each hemisphere. It is worth noting that, in addition to B_z , all other upstream solar wind parameters considered in this study, followed the same behaviour and evolution of that parameter between the quadrants. For both northward and southward IMF, the increase in current magnitude with $|B_z|$ is roughly linear up to $|B_z| \pm 15$ nT. At higher values of B_z , the rate of increase does tend to decrease, but there is no abrupt plateau as seen in studies of CPCP saturation.

3.2 Solar Wind Parameters

The B_z component of the IMF is often considered the most important factor controlling the strength of the solar wind-magnetosphere interaction at Earth. In Figure 3 the behaviour of the current magnitude is presented for instances of both northward (positive values) and southward (negative values) IMF polarity. The B_z range is limited to ± 20 nT as beyond this there are too few observations, during the years 2010-2016, to be statistically significant. The data are grouped into 1 nT bins and the total number of data points in each bin is indicated in panel a of Figure 3. The orange and yellow shading indicates the number of data points, with the scale given in panel e. Figure 3 also shows the variation of three FAC parameters with B_z : the total FAC integrated across the northern hemisphere, the area occupied by these FACs, the mean FAC density (integrated FAC divided by area), in panels b, c and d, respectively. In each AMPERE map, we consider only grid cells with an absolute FAC density greater than 0.1 micro-Amp/m², which is at the noise floor of the AMPERE dataset. We calculate the cross-sectional area occupied by those grid cells and the total absolute FAC (combining upward and downward FACs) and use this area to calculate the mean FAC density as the total integrated FAC divided by the area. This method was used as each the cells do not have a uniform contribution to the total average. The overall distribution of the data is shown by the shading, on a logarithmic scale. We also calculate the mean (red lines) and medians (green circles and diamonds for northward and southward IMF regimes, respectively) in each B_z bin. In panel e we show the distribution of the PC-N index, which we use as a proxy for cross-polar cap potential (e.g. (Milan et al., 2021)). For positive B_z the total FAC, FAC area, and mean FAC density increase linearly with increasing B_z , but the variation is small. The PC-N variation shows no significant variation with positive B_z . A straight blue line is superimposed on the data to help guide the eye. The FAC quantities show a much stronger dependence on negative B_z , as is to be expected. The FAC area increases as the open flux in the polar cap increases, causing the auroral zone expands to lower latitudes and increases in latitudinal extent. The total FAC and mean FAC density also increase, as magnetospheric convection becomes more intense, resulting in stronger FACs

that couple the magnetosphere and ionosphere. However, there are two distinct regimes in the behaviour, with the increase being stronger for $B_z > -10$ nT and weaker for $B_z < -10$ nT. Two blue lines are superimposed to emphasise that the variation is approximately linear in the two regimes, with a distinct knee near $B_z = -10$ nT. PC-N also shows the same behaviour, though the apparent dependence on IMF B_z above and below the knee is less pronounced. We note that, at the time of conducting this study, the PC-N index was only available up to 2014, whereas the AMPERE data used here, covers the period 2010 to 2016. We note, returning to Figure 2, that the knee in the variation of FAC magnitude with negative B_z is apparent in all the individual quadrants as well as the total.

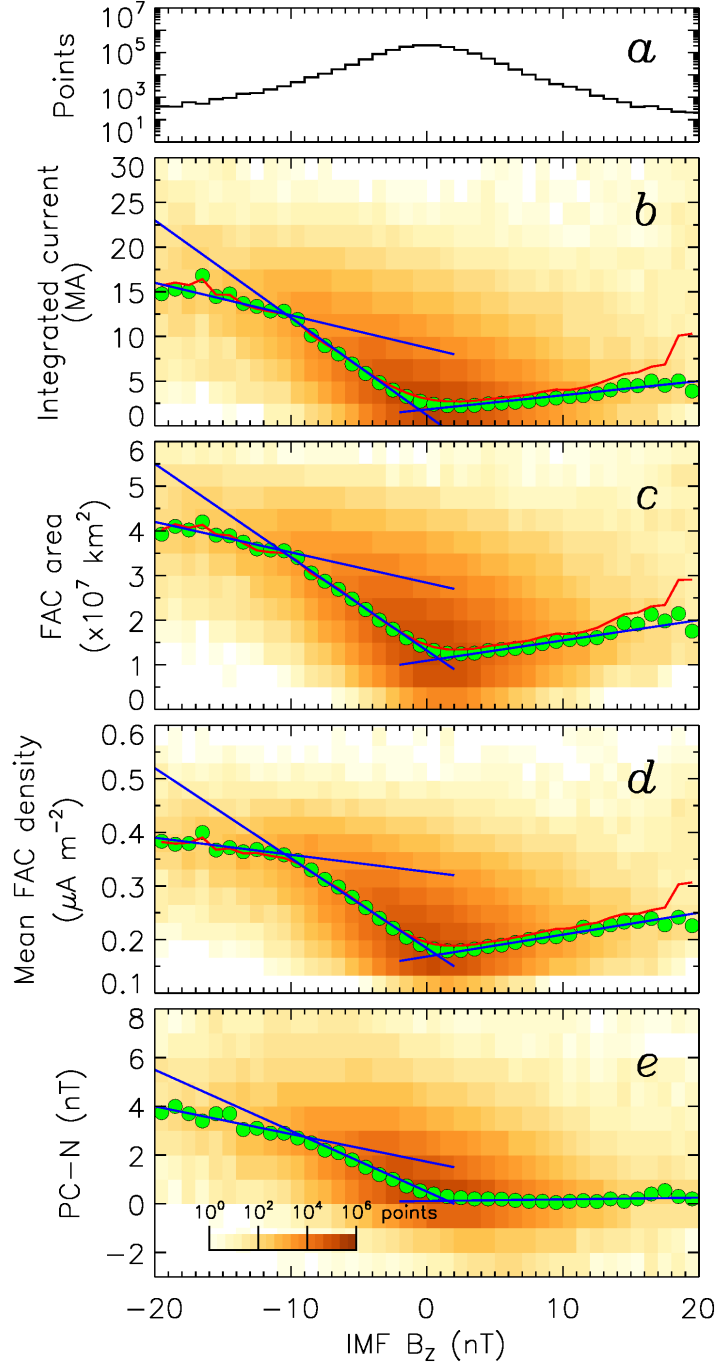


Figure 3. Field aligned current behaviour as a function of the B_z component of the IMF. Each panel shows 1 nT bins of B_z , with panel a indicating the number of data points present in each IMF B_z bin. Panels b,c,d and e show the total integrated current across the northern hemisphere of Earth, the area encompassed by these FACs, the mean FAC density (over the FAC area) and the PC-N index proxy of cross polar cap potential is given (respectively). In each panel, the sum of the upward and downward current is used to give the total integrated current and the shaded orange- yellow colouring gives the distribution of data across the bins. The blue lines on panels b-e are superimposed to guide the eye to the linear behaviour of the data, where applicable and the red lines give the mean. The green markers denote the median of each bin, with a diamond or circular shape denoting southward or northward IMF regimes, respectively.

Figure 4, in the same format as Figure 3, shows the evolution of the same three FAC parameters with increasing solar wind speed. The upper and lower lines show the variation for southward and northward IMF data, indicated by the green diamond and circle markers, respectively.

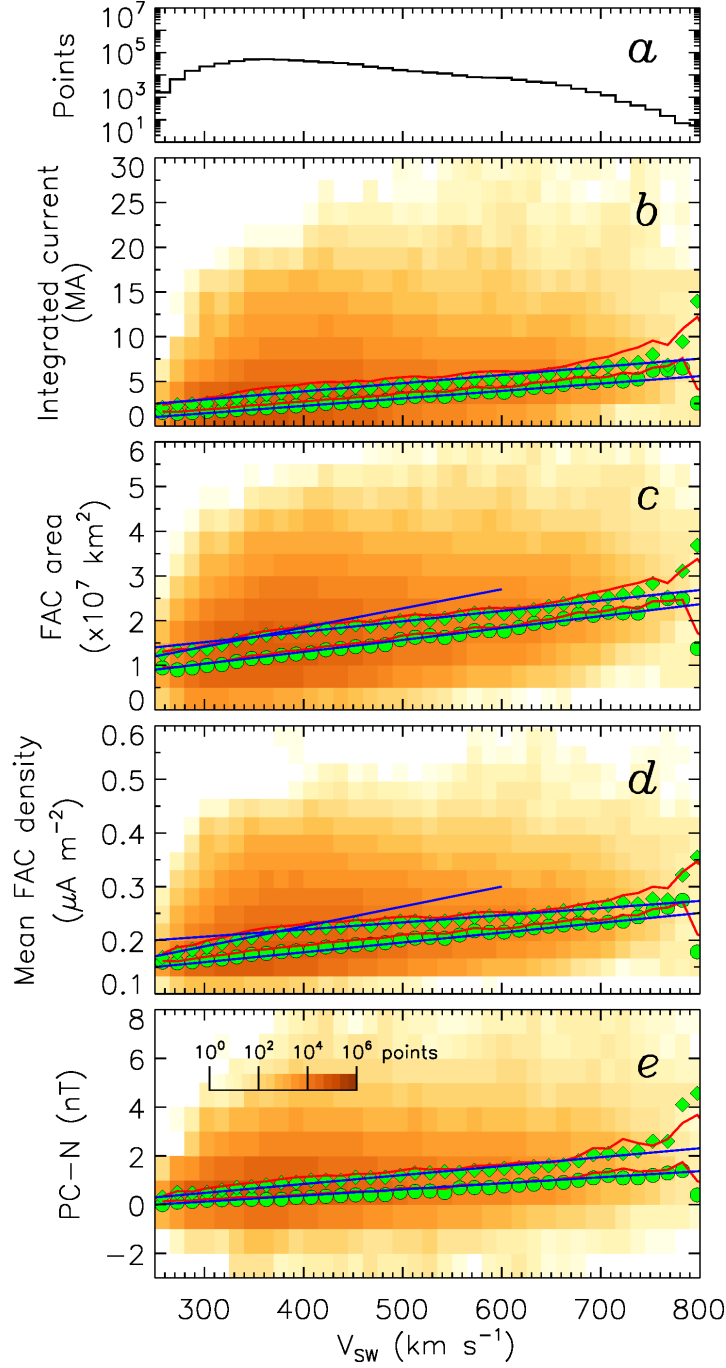


Figure 4. FAC variations with V_{sw} presented in a similar format to Figure 3. The data are subdivided into IMF $B_z < 0$ (upper curve) and $B_z > 0$ (lower curve) and separated into 15 km s^{-1} bins. The blue lines on the lower four panels are superimposed to guide the eye.

The shading indicates the overall distribution of the data, but the mean and medians have been subdivided into IMF $B_z < 0$ (upper curves with diamond shaped markers) and $B_z > 0$ (lower curves with circular shaped markers). The dependence of the FAC parameters on V_{sw} are modest; note that the vertical scales are the same in Figures 3 to 7, indicating the V_{sw} does not order the data particularly well. There is some indication of a knee in the $B_z < 0$ curves of FAC area and density near V_{sw} of 400 km/s, but this is not particularly pronounced. The trend becomes less clear above 700 km/s due to a paucity of data points.

Figure 5 shows the results ordered by N_{sw} for $B_z < 0$ (upper, diamond shaped markers) and $B_z > 0$ (lower, circular shaped markers). As with V_{sw} , the variation of the FAC quantities with N_{sw} is modest and largely linear. The PC-N index is almost independent of N_{sw} .

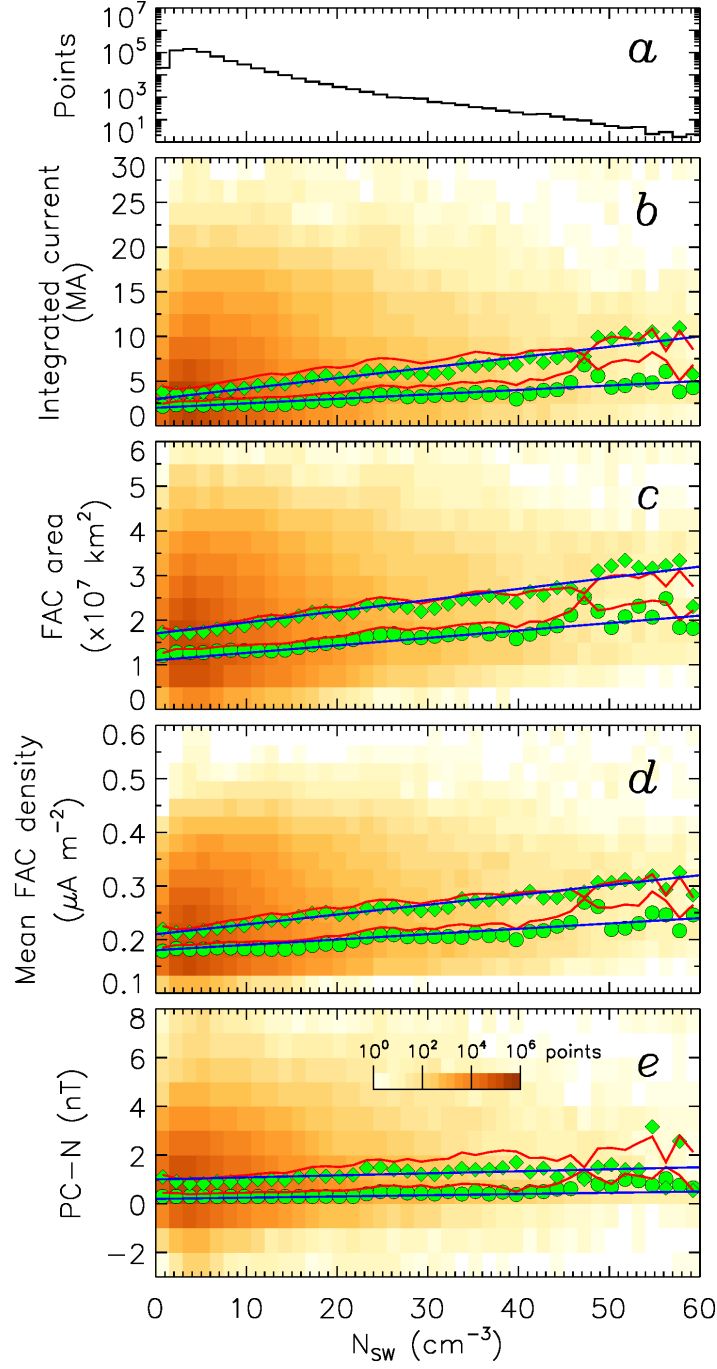


Figure 5. FAC variations with N_{sw} presented in a similar format to Figure 3. The data are subdivided into IMF $B_z < 0$ (upper curve) and $B_z > 0$ (lower curve). Current magnitude behaviour for northwards (upper values) and southwards (lower values) and separated into 1.5 cm^{-3} bins. The blue lines on the lower four panels are superimposed to guide the eye.

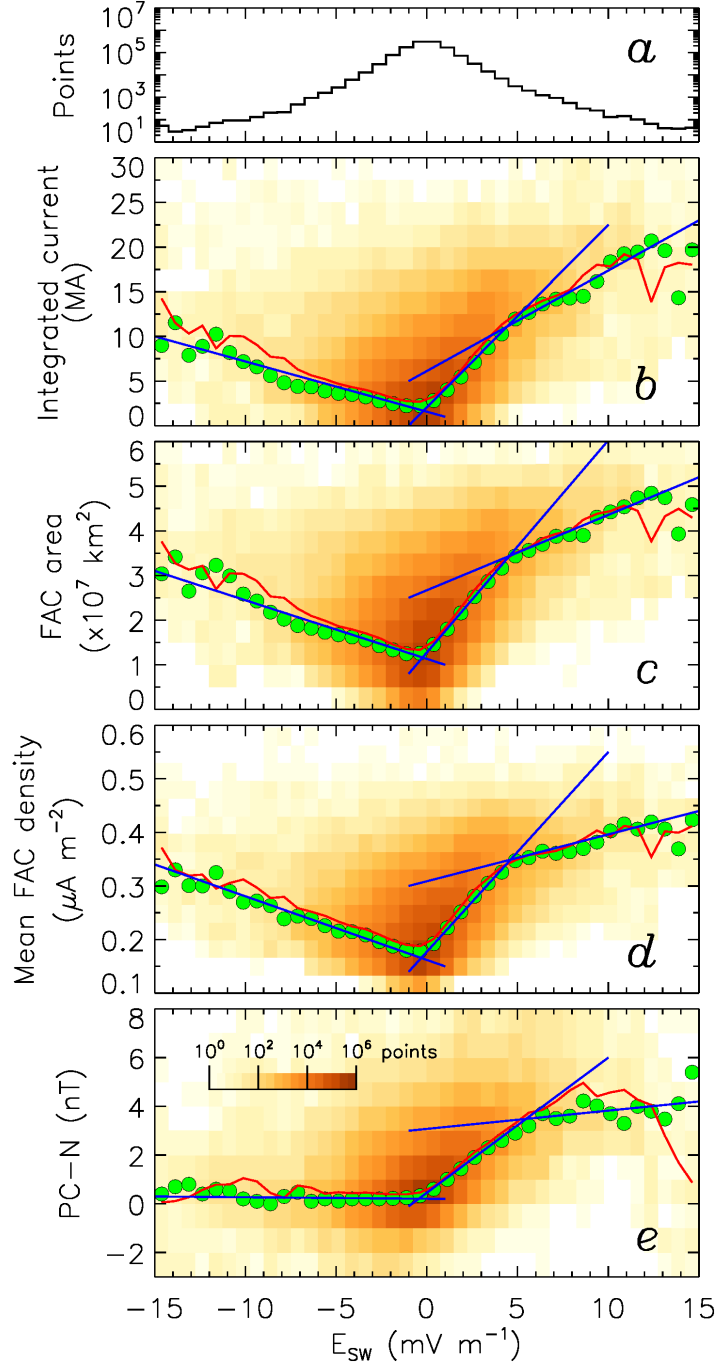


Figure 6. FAC variations with E_{sw} presented in a similar format to Figure 3. The data are subdivided into IMF $B_z < 0$ (positive E_{sw}) and $B_z > 0$ (negative E_{sw}). Current magnitude behaviour for northwards (upper values) and southwards (lower values) and separated into 0.75 mV m^{-1} bins. The blue lines on the lower four panels are superimposed to guide the eye.

Figure 6 presents the variations with E_{sw} . The trends are similar to Figure 3. For $E_{sw} < 0$ ($B_z > 0$), total FAC, FAC area, and FAC density all rise slowly and linearly as the magnitude of E_{sw} increases. For $E_{sw} > 0$, the rise is steeper as the magnitude of E_{sw} increases, but with a distinct knee near $E_{sw} = 4 \text{ mV/m}$, with a slower climb

228 beyond that. Figure 7 presents the relationship of FACs and PC-N to the coupling pa-
 229 rameter shown in equation (1), in a similar format to previous figures. Figure 7 combines
 230 both $B_z > 0$ and $B_z < 0$ values, though $B_z > 0$ will generally give low values of Φ_D
 231 and $B_z > 0$ will give higher values due to the dependence on the IMF clock angle (i.e.,
 232 the $\sin^{\frac{9}{2}} \frac{1}{2} \theta$ term in Equation 1). As in previous figures, a clear knee is seen in all pa-
 233 rameters near 80 to 100 kV.

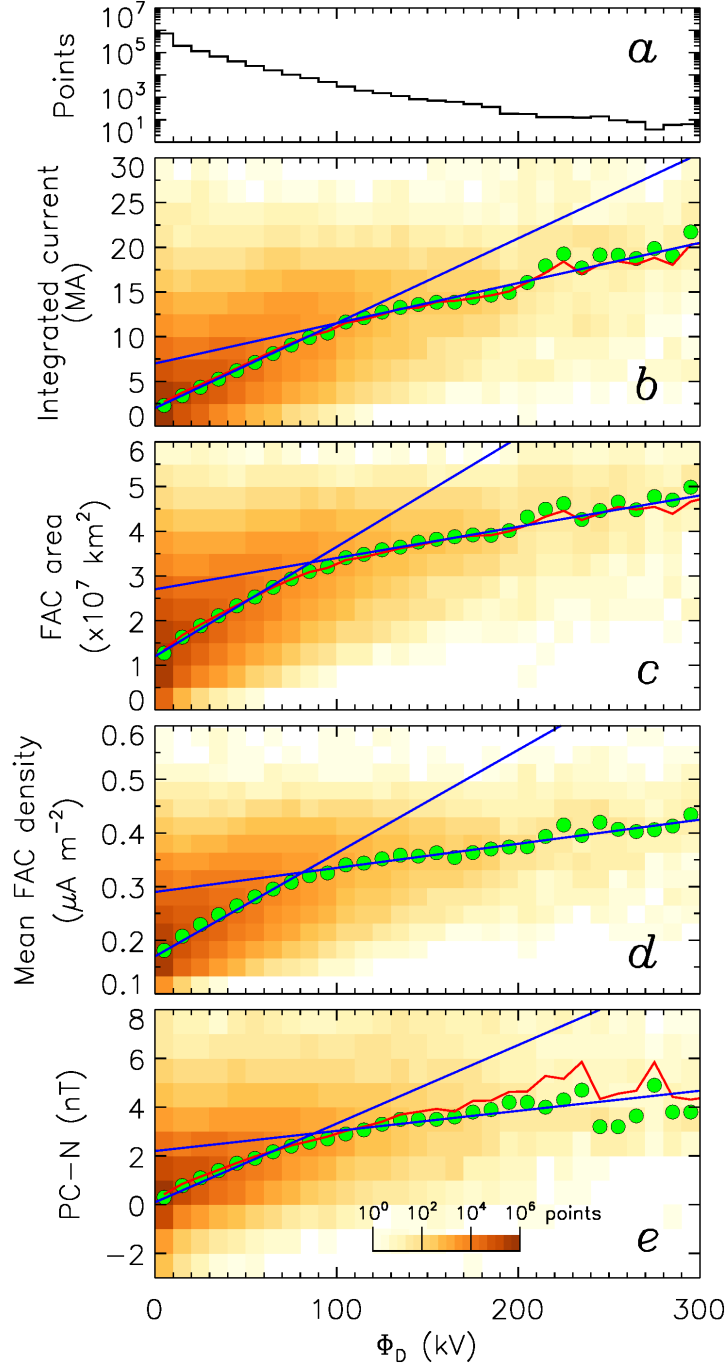


Figure 7. FAC variations with Φ_D , given by the Milan et al. (2012) coupling parameter, presented in a similar format to Figure 3. The Φ_D data are separated into 10 kV bins and the blue lines on the lower four panels are superimposed to guide the eye.

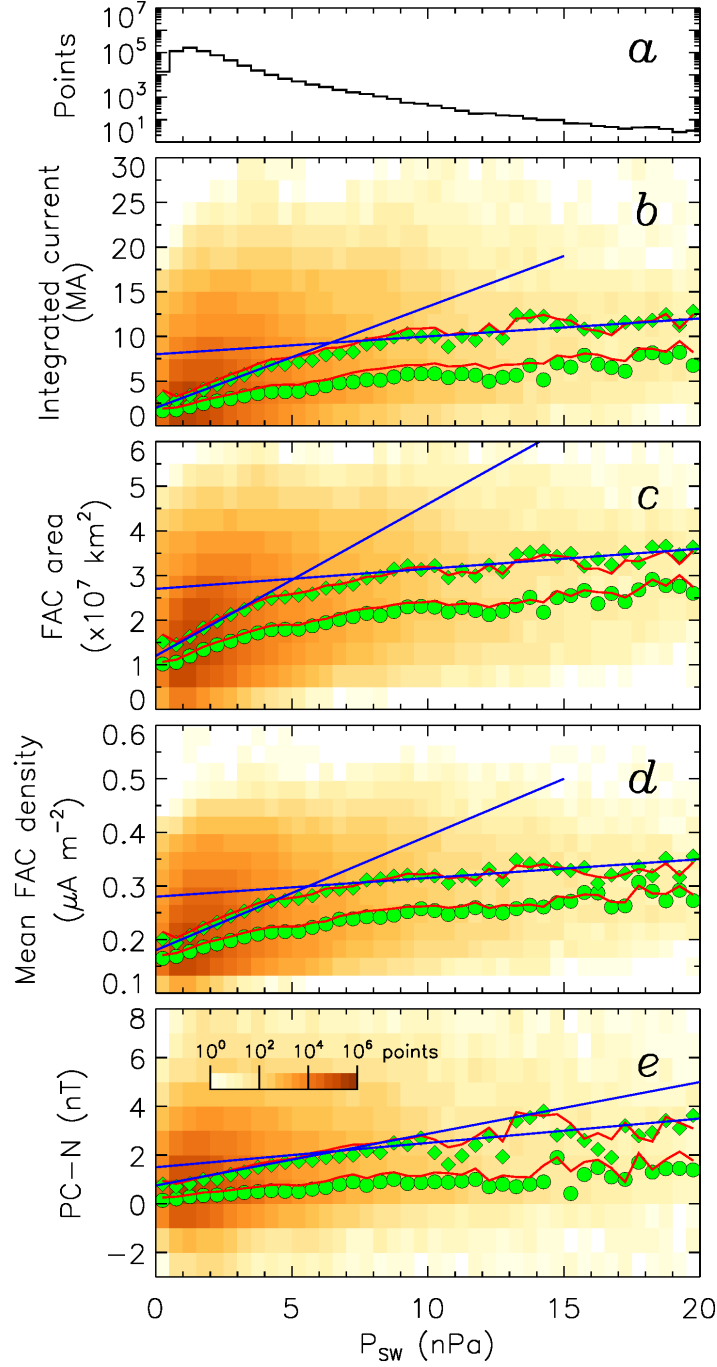


Figure 8. FAC variations with P_{sw} , presented in a similar format to Figure 3. The P_{sw} data are separated into 0.5 nPa bins and the blue lines on panels b-e are superimposed to guide the eye.

The solar wind dynamic pressure (P_{sw}) is given in Figure 8. The increase in P_{sw} shows a knee feature, which has been highlighted on the negative B_z trace (denoted by the diamond markers). It is worth noting here that the linear lines, drawing the eye to the two different regimes of increases is only plotted on the upper curve (southward, diamond marker indicated, IMF), for clarity. The ratio between the two regimes and the linear lines themselves were very similar for both northward and southward IMF.

In many of the presented cases, for IMF $B_z < 0$ there is a distinct knee in the rate of increase in the FAC parameters with increasing solar wind driving. We now compare the rate of increase below the knee (rapid) with the rate above the knee (slow) by taking the ratio of the blue lines fitted above and below the knee. The larger this number, the more distinct is the change in dependencies of FAC parameters on upstream driving conditions. The results are presented in Table 1.

Table 1. Ratio of linear line fits for each parameter regime.

	Φ_D	B_z	E_{sw}	P_{sw}
Area	3.6	3.1	2.8	7.6
Total	2.1	3.0	1.8	5.8
Density	4.3	5.3	4.3	6.0
PC-N	3.9	2.2	7.4	2.1

Across Φ_D , B_z and E_{sw} , the FAC area saw a linearity change ratio of approximately 3. The total integrated current ratio is given to be around 2 for both Φ_D and E_{sw} , however for B_z and P_{sw} the ratio reached 3 and 5.8, respectively. This difference in behaviour of B_z and P_{sw} is also seen in the current density, where the ratios are all generally higher across all parameters, with P_{sw} and B_z still exceeding the values of the other two parameters. PC-N shows the most variability between the three parameters with just 2.1 for P_{sw} and 7.4 for E_{sw} . While P_{sw} and B_z both show a higher change between the pre and post knee regimes, P_{sw} certainly gives the most variation. This is particularly interesting as the constituent parameters of P_{sw} (N_{sw} and V_{sw}) both show no knee feature.

4 Discussion

Within this study, we have investigated how integrated FAC magnitude, area and mean density vary with a variety of solar wind parameters including solar wind speed, density, electric field, B_z component of the IMF and a proxy for solar wind driving (Milan et al. (2012) coupling parameter). During the initial stages of the investigation, the FACs were analysed in 4 separate MLT quadrants in order to identify any unique behaviour of specific current systems, indicated by evolution of current within the specific MLT region. After reviewing each upstream solar wind parameter considered it was found that the resulting current magnitudes in each quadrant, while each having different magnitude contributions to the total, (as would be expected), showed no significant or unique behaviours in any individual MLT quadrant. This uniformity in current evolution allowed the total integrated current across each hemisphere to be used for the analysis. These total current results show that, as the solar wind driving increases and becomes more intense, both the area and the mean density of the FACs increase. The increase in area arises as the FACs move to lower latitudes and have a greater latitudinal width. The increase in FAC density can be attributed to increased coupling at the nose of the magnetosphere increasing open flux and more activity occurring within the magnetotail, resulting in increased particle precipitation and faster ionospheric convection overcoming frictional drag with the atmosphere. While we have employed the Milan et al. (2012) coupling parameter, other coupling parameters have been presented in previous studies, such as the ϵ parameter given in work by Perrault and Akasofu (1978), in addition to the Newell et al. (2007) ‘almost universal’ coupling parameter. Future work may could perform similar analyses using these, and other, coupling parameters in order to gain a greater un-

derstanding of how the trends vary when incorporating different proxies for solar wind driving, in different configurations in terms of solar wind parameters. In this way, an expansion of the previous work of Borovsky (2021), who looked into the varying components of cross polar cap potential saturation.

The solar wind parameters and PC-N has a linear relationship with solar wind speed, V_{sw} . This may suggest that the magnetic field, especially the B_z component is more important in the control of this driving of the FACs. In addition, during periods of northwards IMF (when $B_z > 0$), the FACs increase linearly for stronger B_z and also E_{sw} however this increase is also low. The area of the FACs remains generally quite low, as they are largely confined to the noon sector (as outlined by Figure 1), where lobe reconnection drives reverse convection. The increase in E_{sw} is also seen to be stronger than that of B_z , indicating that the combination of B_z and V_{sw} has greater significance in the driving of lobe reconnection. In addition, it is interesting to note that, while the knee feature is not seen in N_{sw} or V_{sw} , however is evident in the P_{sw} evolution. For all values of $B_z > 0$ (and $E_{sw} < 0$), PC-N remains close to zero. This suggests that PC-N is a poor measure of reverse lobe convection in the noon sector, perhaps due to it being mainly measured within the central polar cap. For $B_z < 0$, the FACs and PC-N increase more strongly, however there is a distinct knee in the variation with B_z , E_{sw} and Φ_D , near -10 nT, 4 mV/m and 90 kV, respectively in each case. These are approximately consistent as combined values of solar wind speed and IMF B_z of 400 km s^{-1} and -10 nT correspond to an E_{sw} of 4 mV/m. The shape of the curves is also approximately consistent with the Hill-Siscoe model presented in (Hairston et al., 2005). For the B_z , E_{sw} and Φ_D parameters, the ratio of the gradients of the blue lines tends to be greatest for FAC density, that is to say that the 'saturation' for this parameter is sharpest, rather than the area or total magnitudes. This could be suggestive that the magnetosphere-ionosphere coupling is limited by the capacity of the magnetosphere to carry current in a given area.

In figures 6 and 7, the FACs do not appear to saturate for $B_z > 0$, as they do for $B_z < 0$. In one regard, $B_z < 0$ does not see the integrated FAC magnitudes and densities reaching as high as the knee feature seen for $B_z < 0$, which may mean they do not reach their limiting value. This is supported by the work of Wilder et al. (2008), which verified a cross polar cap potential saturation during $B_z > 0$ conditions. On the other hand, the Hill-Siscoe model suggests that saturation is caused by a deformation of magnetic structure, and hence reconnection rates, by intense R1 currents, and these are only present for $B_z < 0$. Future work could look at this in more detail by investigating the R1 FACs in isolation and their relationship to other FACs, perhaps using the principal component analysis technique of (Milan et al., 2015). Turning our attention now to the PC-N index, this does not increase with N_{sw} , as predicted by Milan et al. (2012). However, FAC parameters do increase marginally, suggesting that the compression of the magnetosphere somewhat enhances the FACs. This may explain why some coupling parameters find a link between geomagnetic activity and N_{sw} which is not an effect of increased reconnection.

It is important to consider the dynamics of how the FACs are driven when looking at the values within Table 1. Table 1 gives insight into the knee feature seen in the four parameters listed, across all the current values. In particular, the current density shows a consistently high knee feature for all parameters within the table. This would infer that in general, the current density often shows a significant difference in magnitude between the two regimes (before and after the knee feature) for these solar wind parameters (B_z , E_{sw} , P_{sw} and Φ_D). P_{sw} has a high ratio for all parameters, except for PC-N. The solar wind pressure, particularly in the form of pressure pulses, can drive FAC magnitudes and, as such, these high ratios would suggest that this driving can offer a modest contribution, however is limited and will cease to provide additional contributions after the magnitude at which the knee feature occurs. P_{sw} shows the most con-

sistently high change due to the knee feature seen, except for PC-N, indicative of a low dependency of PC-N on P_{sw} . In contrast, the lower ratio values for B_z , such as that for PC-N, are representative of a consistently high dependency on B_z , that continues throughout the knee feature.

5 Conclusion

In this paper we have presented our investigations into saturation across the large-scale FACs of Earth. By using AMPERE data to calculate the total integrated current in each hemisphere, we have analysed the extent of FAC saturation in relation to the upstream solar wind conditions, including parameters such as solar wind speed, density, pressure, B_z component of the IMF, E_{sw} and the Milan et al. (2012) coupling parameter. The currents themselves were also further analysed in terms of total current, mean current density, area over which they cover and also the PC-N index. Consideration was taken to resolve any unique features that may appear in the evolution of the current systems. This was achieved by considering each current system for both northward and southward IMF conditions and based on MLT location. It was concluded, after investigating each parameter, that despite expected differences in overall magnitude, no individual current systems showed any evolution behaviour that would be lost by using the total integrated current. In general, as solar wind driving by all parameters increases, so too does all parameters of the FACs present. This increase can be divided into approximately linear regimes. While some solar wind components (such as V_{sw} and N_{sw}) increase approximately linearly, others show a clear deviation from linearity in the form of a knee feature once the upstream conditions become large enough. The parameters with this feature include E_{sw} , B_z and Φ_D and while they do show a change in behaviour, they do not exhibit the same complete saturation expected from previous studies (Hairston et al., 2005; Shepherd, 2007; Russell et al., 2001).

6 Acknowledgements

A. Fleetham was able to undertake this study, with the support of the co-authors listed, under the financial support of a studentship provided by the Science and Technology facilities council (STFC) as part of UK Research and Innovation (UKRI).

7 Data Availability Statement

The data used within this study can be found in two separate databases. Firstly, the 1-minute resolution solar wind data used can be accessed from OMNIWeb via the link https://omniweb.gsfc.nasa.gov/form/omni_min.html. The 2-minute resolution current map data (AMPERE data) can be retrieved from <https://ampere.jhuapl.edu/download/> with additional tools to help utilise the data available under the 'data tools' tab. In addition, we would like to acknowledge that this research used the SPECTRE High Performance Computing Facility at the University of Leicester. Finally, the authors would like to thank all the teams involved in providing and managing the data and computing services used within this study.

References

- Anderson, B. J., & Korth, H. (2007). Saturation of global field aligned currents observed during storms by the iridium satellite constellation [Journal Article]. *Journal of atmospheric and solar-terrestrial physics*, 69(1), 166-169. doi: 10.1016/j.jastp.2006.06.013
- Anderson, B. J., Takahashi, K., Kamei, T., Waters, C. L., & Toth, B. A. (2002). Birkeland current system key parameters derived from iridium observations:

- Method and initial validation results [Journal Article]. *Journal of Geophysical Research*, 107(A6), SMP 11-1-SMP 11-13. doi: 10.1029/2001JA000080
- Borovsky, J. E. (2021). On the saturation (or not) of geomagnetic indices [Journal Article]. *Frontiers in astronomy and space sciences*, 8. doi: 10.3389/fspas.2021.740811
- Coxon, J. C., Milan, S. E., carter, J. A., Clausen, L. B. N., & Anderson, B. J. (2016). Seasonal and diurnal variations in ampere observations of the birkeland currents compared to modeled results [Journal Article]. doi: JournalofGeophysicalResearch:SpacePhysics,2016,121,doi:10.1002/2015JA0220502169-9402http://onlinelibrary.wiley.com/doi/10.1002/2015JA022050/abstracthttp://hdl.handle.net/2381/3768210.1002/2015JA022050
- Erickson, G. M., Spiro, R. W., & Wolf, R. A. (1991). The physics of the harang discontinuity [Journal Article]. *Journal of Geophysical Research: Space Physics*, 96(A2), 1633-1645. Retrieved from <https://agupubs.onlinelibrary.wiley.com/doi/abs/10.1029/90JA02344> doi: <https://doi.org/10.1029/90JA02344>
- Fear, R. C. (2021). The northward imf magnetosphere [Book Section]. In *Magnetospheres in the solar system* (p. 293-309). Retrieved from <https://agupubs.onlinelibrary.wiley.com/doi/abs/10.1002/9781119815624.ch19> doi: <https://doi.org/10.1002/9781119815624.ch19>
- Fuselier, S. A. (2021). Dayside magnetopause processes [Book Section]. In *Magnetospheres in the solar system* (p. 153-161). Retrieved from <https://agupubs.onlinelibrary.wiley.com/doi/abs/10.1002/9781119815624.ch10> doi: <https://doi.org/10.1002/9781119815624.ch10>
- Ganushkina, N. Y., Liemohn, M. W., & Dubyagin, S. (2018). Current systems in the earth's magnetosphere [Journal Article]. *Reviews of Geophysics*, 56(2), 309-332. Retrieved from <https://agupubs.onlinelibrary.wiley.com/doi/abs/10.1002/2017RG000590> doi: <https://doi.org/10.1002/2017RG000590>
- Gao, Y., Kivelson, M. G., & Walker, R. J. (2013). Two models of cross polar cap potential saturation compared: Siscoe-hill model versus kivelson-ridley model [Journal Article]. *Journal of geophysical research. Space physics*, 118(2), 794-803. doi: 10.1002/jgra.50124
- Hairston, M. R., Drake, K. A., & Skoug, R. (2005). Saturation of the ionospheric polar cap potential during the october–november 2003 superstorms [Journal Article]. *Journal of Geophysical Research: Space Physics*, 110(A9), A09S26-n/a. doi: 10.1029/2004JA010864
- Iijima, T., & Potemra, T. A. (1976a). *The amplitude distribution of field-aligned currents at northern high latitudes observed by triad* (Report).
- Iijima, T., & Potemra, T. A. (1976b). *The amplitude distribution of field-aligned currents at northern high latitudes observed by triad* (Report).
- Khachikjan, G. Y., Koustov, A. V., & Sofko, G. J. (2008). Dependence of superdarn cross polar cap potential upon the solar wind electric field and magnetopause subsolar distance: Cross-polar cap potential saturation [Journal Article]. *Journal of Geophysical Research: Space Physics*, 113(A9), n/a. doi: 10.1029/2008JA013107
- King, J. H., & Papitashvili, N. E. (2005). Solar wind spatial scales in and comparisons of hourly wind and ace plasma and magnetic field data [Journal Article]. *Journal of Geophysical Research*, 110(A2), A02104-n/a. doi: 10.1029/2004JA010649
- Kivelson, M. G., & Ridley, A. J. (2008). Saturation of the polar cap potential: Inference from alfvén wing arguments [Journal Article]. *Journal of Geophysical Research - Space Physics*, 113(A5), A05214-n/a. doi: 10.1029/2007JA012302
- Milan, S. E., Carter, J. A., Bower, G. E., Imber, S. M., Paxton, L. J., Anderson, B. J., ... Hubert, B. (2020). Dual-lobe reconnection and horse-collar auroras [Journal Article]. *Journal of geophysical research. Space physics*, 125(10), n/a.

- doi: 10.1029/2020JA028567
- Milan, S. E., Carter, J. A., Korth, H., & Anderson, B. J. (2015). Principal component analysis of birkeland currents determined by the active magnetosphere and planetary electrodynamics response experiment: Principal component analysis of facs [Journal Article]. *Journal of geophysical research. Space physics*, 120(12), 10-10,424. doi: 10.1002/2015JA021680
- Milan, S. E., Carter, J. A., Sangha, H., Bower, G. E., & Anderson, B. J. (2021). Magnetospheric flux throughput in the dungey cycle: Identification of convection state during 2010 [Journal Article]. *Journal of geophysical research. Space physics*, 126(2), n/a. doi: 10.1029/2020JA028437
- Milan, S. E., Clausen, L. B. N., Coxon, J. C., Carter, J. A., Walach, M. T., Laundal, K., ... Anderson, B. J. (2017). Overview of solar wind-magnetosphere-ionosphere-atmosphere coupling and the generation of magnetospheric currents [Journal Article]. *Space science reviews*, 206(1-4), 547-573. doi: 10.1007/s11214-017-0333-0
- Milan, S. E., Gosling, J. S., & Hubert, B. (2012). Relationship between interplanetary parameters and the magnetopause reconnection rate quantified from observations of the expanding polar cap [Journal Article]. *Journal of Geophysical Research: Space Physics*, 117(A3), n/a. doi: 10.1029/2011JA017082
- Newell, P. T., Sotirelis, T., Liou, K., Meng, C. I., & Rich, F. J. (2007). A nearly universal solar wind-magnetosphere coupling function inferred from 10 magnetospheric state variables [Journal Article]. *Journal of Geophysical Research: Space Physics*, 112(A1), A01206-n/a. doi: 10.1029/2006JA012015
- Perrault, P., & Akasofu, S.-I. (1978). A study of geomagnetic storms. [Journal Article]. *Geophysics Journal of the Royal Astronomical Society Special Publications*, 54.
- Russell, C. T., Luhmann, J. G., & Lu, G. (2001). Nonlinear response of the polar ionosphere to large values of the interplanetary electric field [Journal Article]. *Journal of Geophysical Research: Space Physics*, 106(A9), 18495-18504. doi: 10.1029/2001JA900053
- Shepherd, S. G. (2007). Polar cap potential saturation: Observations, theory, and modeling [Journal Article]. *Journal of atmospheric and solar-terrestrial physics*, 69(3), 234-248. doi: 10.1016/j.jastp.2006.07.022
- Siscoe, G. L., Erickson, G. M., Sonnerup, B. U., Maynard, N. C., Schoendorf, J. A., Siebert, K. D., ... Wilson, G. R. (2002). Hill model of transpolar potential saturation: Comparisons with mhd simulations [Journal Article]. *Journal of Geophysical Research*, 107(A6), SMP 8-1-SMP 8-8. doi: 10.1029/2001JA000109
- Waters, C. L., Anderson, B. J., Green, D. L., Korth, H., Barnes, R. J., & Vanhamäki, H. (2020). Science data products for ampere [Book Section]. In M. W. Dunlop & H. Lüher (Eds.), *Ionospheric multi-spacecraft analysis tools: Approaches for deriving ionospheric parameters* (p. 141-165). Cham: Springer International Publishing. Retrieved from https://doi.org/10.1007/978-3-030-26732-2_7 doi: 10.1007/978-3-030-26732-2_7
- Waters, C. L., Anderson, B. J., & Liou, K. (2001). Estimation of global field aligned currents using the iridium® system magnetometer data [Journal Article]. *Geophysical Research Letters*, 28(11), 2165-2168. Retrieved from <https://agupubs.onlinelibrary.wiley.com/doi/abs/10.1029/2000GL012725> doi: <https://doi.org/10.1029/2000GL012725>
- Wilder, F. D., Clauer, C. R., & Baker, J. B. H. (2008). Reverse convection potential saturation during northward imf: Reverse convection saturation [Journal Article]. *Geophysical research letters*, 35(12), n/a. doi: 10.1029/2008GL034040
- Zanetti, L. J., Potemra, T. A., Iijima, T., Baumjohann, W., & Bythrow, P. F. (1984). Ionospheric and birkeland current distributions for northward interplanetary magnetic field: Inferred polar convection [Journal Article]. *Jour-*

488 *nal of Geophysical Research: Space Physics*, 89(A9), 7453-7458. Retrieved
489 from [https://agupubs.onlinelibrary.wiley.com/doi/abs/10.1029/](https://agupubs.onlinelibrary.wiley.com/doi/abs/10.1029/JA089iA09p07453)
490 JA089iA09p07453 doi: <https://doi.org/10.1029/JA089iA09p07453>